applied sciences

MDPI

Communication

Research on the Image-Motion Compensation Technology of the Aerial Camera Based on the Multi-Dimensional Motion of the Secondary Mirror

Hongwei Zhang *, Rui Qu, Weining Chen and Huinan Guo

Xi'an Institute of Optics and Precision Mechanics, Chinese Academy of Sciences, Xi'an 710119, China; qurui@opt.ac.cn (R.Q.); cwn@opt.ac.cn (W.C.); guohuinan@opt.ac.cn (H.G.)
* Correspondence: zhanghongwei@opt.ac.cn

Abstract: Targeting the dynamic image-motion problem of aerial cameras in the process of swing imaging, the image-motion compensation technology of aerial cameras based on the multi-dimensional motion of the secondary mirror was adopted. The secondary mirror was used as the image-motion compensation element, and the comprehensive image-motion compensation of the aerial camera was realized through the multi-dimensional motion of the secondary mirror. However, in the process of compensating for the image motion, the secondary mirror would be eccentric and inclined, which would cause the secondary mirror to be off-axis and affect the image quality. Therefore, a misalignment optical system model was established to study the relationship between the deviation vector and the misalignment of the secondary mirror, and the influence of the secondary mirror's motion on the distribution of the aberration was analyzed. In order to verify the image-motion compensation ability of the multi-dimensional motion of the secondary mirror, an experimental platform was built to conduct a laboratory imaging experiment and flight experiment on the aerial camera. The experimental results showed that the dynamic resolution of the aerial camera using the image-motion compensation technology could reach 74 lp/mm, and the image-motion compensation accuracy was better than 0.5 pixels, which met the design expectation. In conclusion, the image-motion compensation technology is expected to be applied to various high-precision optical imaging as well as optical detection systems.

Keywords: aerial camera; image-motion compensation technology; secondary mirror multi-dimensional motion; vector aberration theory

check for updates

Citation: Zhang, H.; Qu, R.; Chen, W.; Guo, H. Research on the Image-Motion Compensation Technology of the Aerial Camera Based on the Multi-Dimensional Motion of the Secondary Mirror. *Appl. Sci.* **2024**, *14*, 7079. https://doi.org/10.3390/app14167079

Academic Editor: Atsushi Mase

Received: 1 July 2024
Revised: 23 July 2024
Accepted: 8 August 2024
Published: 12 August 2024

Copyright: © 2024 by the authors. Licensee MDPI, Basel, Switzerland. This article is an open access article distributed under the terms and conditions of the Creative Commons Attribution (CC BY) license (https://creativecommons.org/licenses/by/4.0/).

1. Introduction

To achieve high-resolution aerial imaging, aerial cameras need longer focal length optical lenses, which will result in a smaller field of view (FOV) and narrower imaging width, thus reducing the efficiency of practical applications. To solve this problem, aerial mapping cameras can adopt a scanning imaging mode [1–4]. However, this imaging mode can cause scanning image-motion problems. Considering the characteristics of the airborne platform, the image motions of aerial cameras mainly include the aircraft attitude image motion, vibration image motion, forward image motion, and scanning image motion.

The large motion of the image will significantly impact the imaging quality of the system, leading to issues such as image trailing, blurred contours, and overlapping details, and ultimately resulting in a significant decrease in image resolution [5,6]. The phenomenon of carrier attitude image motion refers to the image motion that occurs as a consequence of a change in carrier attitude at the time of the camera exposure. The size of the image motion is contingent upon the carrier flight status and the camera exposure time, and it can be compensated for by a two-dimensional stable platform. Vibrational image motion is the image motion caused by the vibration of the airborne platform itself, transmitted to the camera system. Compared with other image motions, this image motion belongs

to a high-frequency image motion. By choosing a vibration damping system that does not exhibit angular displacement, with an appropriate stiffness and damping ratio, the angular displacement that has a significant impact on imaging can be converted to a linear displacement that has a minimal impact on imaging, thus reducing or even eliminating the vibration image motion. However, the working mechanism of the camera's scanning imaging determines that large image motions in both the flight and scanning directions are inevitable. In order to minimize the impact of these motions on imaging quality to an acceptable level, it is necessary to analyze and compensate for the imaging motions of the camera, thereby reducing their effect on imaging and ensuring the camera's imaging capability.

Currently, Raytheon's Global Hawk camera, Recon Optical, Inc.'s CA-295, Goodrich's DB-110, L3Harris Technologies' LOROP, and VisionMap Company's VisionMap A3 are the mainstream airborne cameras with advanced performance. Among them, CA-295, DB-110, and LOROP utilize a multi-axis stabilized platform and optical system to achieve image-motion compensation. The Global Hawk camera adopts the composite control technology of visual axis with continuous scanning of the primary mirror and synchronous movement of the built-in mirror to realize image-motion compensation. The VisionMap A3 employs multi-dimensional motions of the secondary mirror to realize comprehensive image-motion compensation. This highly integrated design concept of optical imaging and image-motion compensation has the effect of simplifying the complexity of the optical imaging system, which in turn facilitates the compact and lightweight design of the imaging system. However, due to the particularity of the earth observation field, there is little published literature on this kind of technology.

On this basis, this paper provides an in-depth study of image-motion compensation technology based on the multi-dimensional motion of the secondary mirror, and it realizes high-precision image-motion compensation and pointing measurement through multi-dimensional fast motion of the secondary mirror [7,8]. This technology addresses the challenge of image blurring and distortion caused by the motion of the aircraft during aerial reconnaissance and mapping activities. By compensating for these image motions, the technology ensures that the captured images are of high quality, enabling accurate and reliable mapping and reconnaissance data to be obtained. This in turn enhances the precision and efficiency of aerial surveying and mapping, making significant contributions to various scientific fields such as geospatial analysis, environmental monitoring, and resource management. Additionally, the development and application of this technology also contribute to advancements in remote sensing and aerial imaging techniques, furthering the capabilities and applications of aerial reconnaissance and mapping. Overall, image-motion compensation technology has made substantial scientific contributions by enabling the acquisition of high-quality aerial images for a wide range of scientific and operational purposes.

The rest of this paper is arranged as follows. In Section 2, we analyze and calculate the forward image motion and the scanning motion of an aerial camera under some operating conditions, and the analysis results demonstrate the necessity for image-motion compensation. In Section 3, the image-motion compensation technique based on the multi-dimensional motion of the secondary mirror is studied, then the relationship between the deviation vector and the misalignment of the secondary mirror is studied, and the influence of the secondary mirror's motion on the distribution of the aberration is analyzed. In Section 4, a design case based on the image-motion compensation technique is presented. In Section 5, the actual experimental process is described and the experimental results are discussed. Section 6 presents the conclusions.

2. Necessity Analysis of Image-Motion Compensation

In order to fulfill the requirements of wide-width measurement imaging, the aerial camera employs the scanning imaging mode. This mode ensures that the exposure time and scanning speed of the camera correspond to the necessary requirements for forward overlap rate and lateral overlap rate, which are essential for scale mapping. In order to

ascertain the necessity of image-motion compensation, some flight parameters of an aerial camera were selected as examples, as shown in Table 1, for analysis and calculation of the image motion of the aerial camera in the scanning imaging mode.

Table 1. The flight parameters of an aerial camera.

Parameters		Values
Aircraft platform parameters	Flight altitude	7.50 km
	Flight speed	180 km/h~280 km/h
Camera parameter	Spectrum	435 nm~900 nm
	Focal length (f)	450.00 mm
	Pixel size (ps)	6.40 μm
	FOV	4.17° × 3.13°
	F number	4.20
	MTF	≥0.20 (80 lp/mm @ all FOV)
	Exposure time	1.00 ms
	Scanning range	−60°~+60°
	Forward overlap rate	78%
	Lateral overlap rate	30%

During the aircraft's forward flight, the aerial camera scans and captures images. When the camera is oriented vertically for photography, combined with the parameters in Table 1, the forward image motion and scanning image motion of the aerial camera at the camera exposure time can be calculated theoretically [9–11].

$$S_x = f\dot{\alpha}\tau, \tag{1}$$

$$S_y = f\frac{V_s}{H}\tau, \tag{2}$$

where S_x is the scanning image motion of the aerial camera, S_y is the forward image motion of the aerial camera, f is the focal length, $\dot{\alpha}$ is the scanning angular velocity, τ is the exposure time, V_s is the flight speed, and H is the flight altitude. $\dot{\alpha}$ can be calculated according to the lateral overlap rate, the scanning FOV, and the scanning imaging time.

According to Equations (1) and (2) and the parameters in Table 1, the image motions in both directions at different speed-to-height ratios could be calculated as shown in Table 2.

Table 2. Image motions at different speed-to-height ratios.

Image Motions \ Speed-to-Height Ratios		0.0067	0.0074	0.0081	0.0089	0.0096	0.0104
Forward image motions	μm	3.02	3.34	3.64	4	4.32	4.68
	pixel	0.47	0.52	0.57	0.63	0.68	0.73
Scanning image motions	μm	256.8	285.2	313.4	341.6	370.8	399
	pixel	40.13	44.56	48.97	53.38	57.94	62.34

As illustrated in Table 2, the forward and scanning image motions are positively correlated with the speed-to-height ratio. The maximum forward image motion is 0.73 pixels, while the maximum scanning image motion is 62.34 pixels. These values are greater when the exposure time is longer or when the speed-to-height ratio is greater. In general, when the image motion of the system exceeds 0.5 pixels, the image quality is severely degraded and needs to be compensated for.

3. Image-Motion Compensation Technique of the Secondary Mirror Motion

3.1. Image-Motion Compensation Scheme

In order to achieve high-resolution scanning imaging, aerial cameras must select an appropriate image-motion compensation scheme to overcome the forward and scanning image motions introduced by their own imaging mechanisms. Currently, there are various forms of image-motion compensation schemes commonly used in aerial cameras, which can be broadly categorized as optical image-motion compensation, mechanical image-motion compensation, electronic image-motion compensation, and digital image-motion compensation.

For the current mainstream long focal length, common aperture, and multi-band aerial cameras, the optimal approach is to implement optical image-motion compensation, which adopts the multi-dimensional movement of an optical element to achieve the comprehensive image-motion compensation of multi-band cameras. In addition, during the selection process of the optical element for the image-motion compensation, two points should be emphasized: one is the high efficiency of image-motion compensation, and the other is that the motion of the optical element has the least influence on the image quality. Also worth comprehensive consideration is that the secondary mirror in the catadioptric optical system is used as the optical element for image-motion compensation, and the purpose of comprehensive image-motion compensation is achieved through its multi-dimensional movement. The principle and flow chart of image-motion compensation are shown in Figures 1 and 2 respectively.

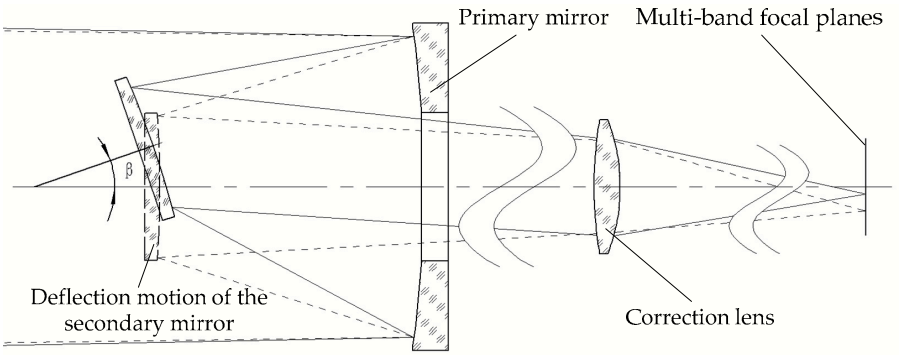

Figure 1. Principle of image-motion compensation.

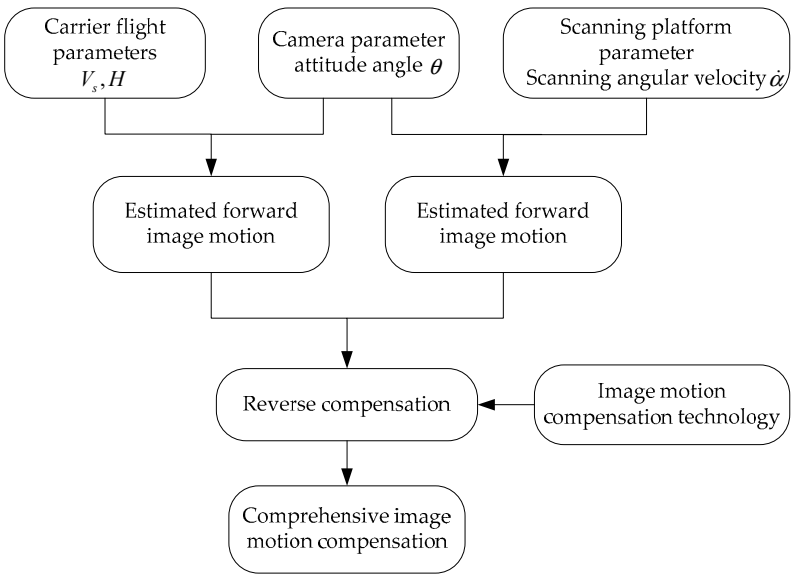

Figure 2. Flow chart of image-motion compensation.

3.2. Aberration Field Constant Technique

The catadioptric optical system typically consists of a two-mirror telescope system and a correction lens. In this optical system, the two-mirror telescope system adopts a Cassegrain structure, and the correction lens adopts a combination of single lenses and a double-glued lens. Considering the universality and applicability of modeling, this paper takes the Cassegrain optical system with aperture stop on the primary mirror as the research object of the secondary mirror for image-motion compensation. During the process of compensating for image motion, the secondary mirror is inevitably eccentric and tilted, resulting in the secondary mirror being off-axis. Once the secondary mirror is off-axis, the optical system loses the original symmetry of the optical system, so the traditional aberration model is no longer applicable and the vector aberration theory must be introduced [12,13].

3.2.1. Secondary Mirror Motion Induces First-Order Effects

In order to elucidate the operational principle of the secondary mirror in compensating for image motion, it is essential to establish a model of the misalignment optical system and investigate the interrelationship between the deviation vector of the secondary mirror and the misalignment of the secondary mirror. The offset of the image point position of the optical system caused by the movement of the secondary mirror can be determined by tracing the optical axis rays to the image plane [14,15], as illustrated in Figure 3.

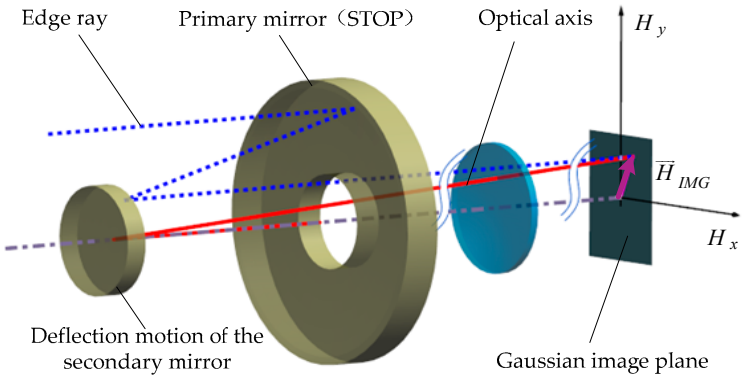

Figure 3. Interrelationship between the deviation vector and the misalignment of the secondary mirror.

According to the theory of the off-axis vector aberration, the offset of the image point position of the optical system caused by the motion of the secondary mirror can be obtained by Equation (3):

$$\vec{H}_{IMG} = \sqrt{\vec{H}_{x_IMG}^{\ 2} + \vec{H}_{y_IMG}^{\ 2}}, \tag{3}$$

where $\vec{H}_{IMG}$ is the offset of the image point position of the optical system, $\vec{H}_{x_IMG}$ is the vector components of the image point position offset in the x-axes, and $\vec{H}_{y_IMG}$ is the vector components of the image point position offset in the y-axes.

In Equation (3), the vector components of the image point position offset in the X and y-axes of the image plane can be expressed as follows:

$$\begin{bmatrix} \vec{H}_{x_IMG} \\ \vec{H}_{y_IMG} \end{bmatrix} = \frac{\beta L(1-m)}{(f'_{SYS})\gamma\overline{y}_{IMG}} \begin{bmatrix} E_{SM_x} - \frac{2\gamma(f'_{SYS})}{1-m}\varphi_{SM_y} \\ E_{SM_y} + \frac{2\gamma(f'_{SYS})}{1-m}\varphi_{SM_x} \end{bmatrix}, \tag{4}$$

$$L = \gamma f'_{SYS}, \tag{5}$$

$$m \equiv -\frac{f'_{SYS}}{f'_{PM}}, \tag{6}$$

where β is the magnification of the correction lens, γ is the blocking ratio, L is the distance from the aspherical vertex of the secondary mirror to the Gaussian image plane, f'_{SYS} is the focal length of the telescope system, f'_{PM} is the focal length of the primary mirror, $\overline{y}_{IMG}$ is the height of the primary optical axis of the image coordinate system, E_{SM_x}/E_{SM_y} is the eccentricity of the secondary mirror, $\varphi_{SM_x}/\varphi_{SM_y}$ is the tilt of the secondary mirror, and m is the ratio of f'_{SYS} to f'_{PM}.

In order to facilitate calculation, Equation (4) is further derived to obtain:

$$\begin{bmatrix} \vec{H}_{x_IMG} \\ \vec{H}_{y_IMG} \end{bmatrix} = \frac{\beta}{\overline{y}_{IMG}} \begin{bmatrix} (1-m)E_{SM_x} - (2L)\varphi_{SM_y} \\ (1-m)E_{SM_y} + (2L)\varphi_{SM_x} \end{bmatrix}, \tag{7}$$

In addition, the center of rotation of the secondary mirror is set as the coma-free pivot point. When the tilt of the secondary mirror is small, according to the geometric relationship shown in Figure 4, the eccentricity of the secondary mirror can be simplified as Equation (8).

$$\begin{bmatrix} E_{SM_x} \\ E_{SM_y} \end{bmatrix} = \begin{bmatrix} L_{SM}^{cfp} \cdot \sin\left(180\varphi_{SM_y}/\pi\right) \\ L_{SM}^{cfp} \cdot \sin\left(180\varphi_{SM_x}/\pi\right) \end{bmatrix} \approx \begin{bmatrix} L_{SM}^{cfp} \cdot \varphi_{SM_y} \\ L_{SM}^{cfp} \cdot \varphi_{SM_x} \end{bmatrix}, \tag{8}$$

where L_{SM}^{cfp} is the distance from the aspherical vertex of the secondary mirror to the center of curvature of the secondary mirror.

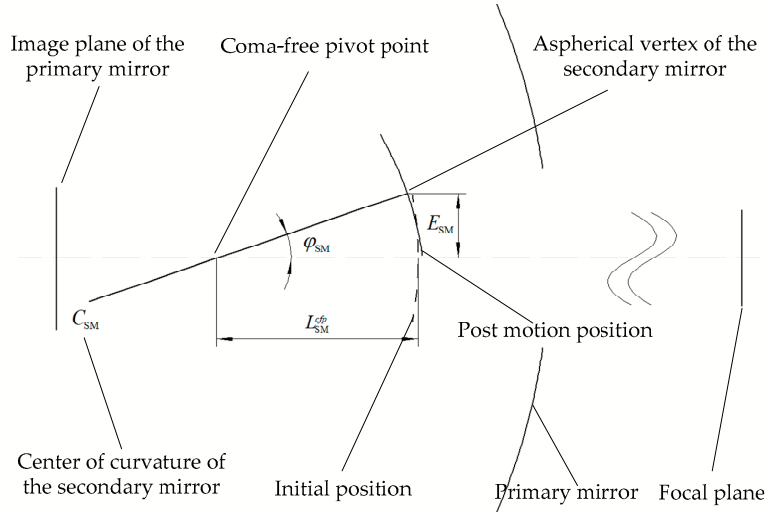

Figure 4. Eccentricity vector introduced by the motion of the secondary mirror.

By substituting Equation (8) into Equation (7), we obtain:

$$\begin{bmatrix} \vec{H}_{x_IMG} \\ \vec{H}_{y_IMG} \end{bmatrix} = \frac{\beta}{\overline{y}_{IMG}} \begin{bmatrix} \left((1-m)L_{SM}^{cfp} - 2L\right)\varphi_{SM_y} \\ \left((1-m)L_{SM}^{cfp} + 2L\right)\varphi_{SM_x} \end{bmatrix}, \tag{9}$$

As illustrated in Equation (9), when the rotation angle of the secondary mirror around the coma-free pivot point is comparatively small, the image point position offset and the secondary mirror deflection angle are linearly correlated. Consequently, when the relationship between the image point position offset and the image motion at the moment of camera exposure aligns with Equation (10), comprehensive compensation for image motion can be attained.

$$\vec{H}_{IMG} = -\vec{H}_{Motion} \tag{10}$$

where $\vec{H}_{Motion}$ is the image motion at the moment of camera exposure.

3.2.2. Secondary Mirror Motion Induces Third-Order Aberrations Effects

Since the third-order spherical aberration is not affected by the size of the FOV, when the motion of the secondary mirror does not change the spacing of the primary mirror and secondary mirror, it does not affect the balance of the third-order spherical aberration of the optical system. The influence of the secondary mirror off-axis on the optical system is mainly manifested in the third-order coma and the third-order astigmatism. The third-order coma is linearly related to the size of the FOV and has only one coma node, and the third-order astigmatism is squared with the size of the FOV and has two astigmatic nodes [16–18].

According to the vector aberration theory, the third-order coma of the misaligned R-C system can be calculated according to Equations (11) and (12).

$$W_{COMA3} = \begin{bmatrix} -\vec{A}_{131,x} \\ -\vec{A}_{131,y} \end{bmatrix} \left[\vec{\rho}\right](\vec{\rho} \cdot \vec{\rho}), \tag{11}$$

$$\begin{bmatrix} \vec{A}_{131,x} \\ \vec{A}_{131,y} \end{bmatrix} = \begin{bmatrix} \vec{\sigma}^{(sph)}_{SM,x} & \vec{\sigma}^{(asph)}_{SM,x} \\ \vec{\sigma}^{(sph)}_{SM,y} & \vec{\sigma}^{(asph)}_{SM,y} \end{bmatrix} \begin{bmatrix} W^{sph}_{131,SM} \\ W^{asph}_{131,SM} \end{bmatrix}, \tag{12}$$

where W_{COMA3} is the third-order coma, $\vec{A}_{131,x}/\vec{A}_{131,y}$ is the constant coma of the field of view, $\vec{\rho}$ is the pupil vector, W_{131} is the coefficient of the third-order coma, $\vec{\sigma}^{(sph)}_{SM,x}/\vec{\sigma}^{(sph)}_{SM,y}$ is the normalized spherical aberration eccentricity vector, and $\vec{\sigma}^{(asph)}_{SM,x}/\vec{\sigma}^{(asph)}_{SM,y}$ is the normalized aspheric aberration eccentricity vector.

Applying the same method, the third-order astigmatism of the misaligned R-C system is given by the following equation:

$$W_{ATS3} = \frac{1}{2}\left[W_{222}\vec{H}^{2} - 2\vec{H}\vec{A}_{222} + \vec{B}^{2}_{222}\right](\vec{\rho}^{2}), \tag{13}$$

where W_{ATS3} is the third-order astigmatism, $\vec{H}$ is the FOV vector, and W_{222} is the coefficient of the third-order astigmatism.

Define $\vec{A}_{222}$ and $\vec{B}^{2}_{222}$ as follows:

$$\begin{bmatrix} \vec{A}_{222,x} \\ \vec{A}_{222,y} \\ \vec{B}^{2}_{222,x} \\ \vec{B}^{2}_{222,y} \end{bmatrix} = \begin{bmatrix} \vec{\sigma}^{(sph)}_{SM,x} & \vec{\sigma}^{(asph)}_{SM,x} \\ \vec{\sigma}^{(sph)}_{SM,y} & \vec{\sigma}^{(asph)}_{SM,y} \\ \vec{\sigma}^{(sph)2}_{SM,x} - \vec{\sigma}^{(sph)2}_{SM,y} & \vec{\sigma}^{(asph)2}_{SM,x} - \vec{\sigma}^{(asph)2}_{SM,y} \\ 2\vec{\sigma}^{(sph)}_{SM,x}\vec{\sigma}^{(sph)}_{SM,y} & 2\vec{\sigma}^{(asph)}_{SM,x}\vec{\sigma}^{(asph)}_{SM,y} \end{bmatrix} \begin{bmatrix} W^{sph}_{222,SM} \\ W^{asph}_{222,SM} \end{bmatrix}, \tag{14}$$

The third-order astigmatism induced by the secondary mirror off-axis exhibits a two-nodes phenomenon [19], and the position of the astigmatic nodes $\vec{H}_{ATS3}$ in the FOV can be determined using Equation (15).

$$\vec{H}_{ATS3} = \frac{\vec{A}_{222}}{W_{222}} \pm i\sqrt{\frac{\vec{B}^{2}_{222}}{W_{222}} - \left(\frac{\vec{A}_{222}}{W_{222}}\right)^{2}}, \tag{15}$$

where $\frac{\vec{A}_{222}}{W_{222}}$ is a vector from the intersection of the optical axis and the image plane to the midpoint of the line between the two astigmatic nodes, and $\pm i\sqrt{\frac{\vec{B}_{222}^{2}}{W_{222}} - \left(\frac{\vec{A}_{222}}{W_{222}}\right)^{2}}$ are two vectors that point from the end point of the $\frac{\vec{A}_{222}}{W_{222}}$ vector to the two astigmatic nodes.

4. Design Case

Based on the research and analysis in this paper, a catadioptric optical system was designed with imaging and a motion-compensation function of the secondary mirror. The focal length of the catadioptric optical system was 450 mm, the spectral range was 435 nm~900 nm, the F number was 4.2, and the FOV of the optical system was 4.17° × 3.13°. The specific parameters were shown in Table 1.

The optical system was designed with a catadioptric structural form, which allowed for the off-axis complication of the secondary mirror. The two-mirror telescope system of the optical system was constructed in the form of an R-C structure [20–25]. A correction lens was positioned between the secondary mirror and the focal plane, thereby increasing the field of view of the optical system. The TF3 special glass was employed for the purpose of correcting the secondary spectrum [26–29]. Through the matching of optical materials and structural materials, the athermalization design of the optical imaging system was realized [30–32]. The optical system employed spectroscopic prisms to segregate panchromatic light into four distinct spectral bands, namely R, G, B and NIR, and then imaged them individually. The optical system adopted the multi-dimensional movement of the secondary mirror to achieve comprehensive image-motion compensation of the four spectral bands cameras. The final design results are shown in Figures 5 and 6.

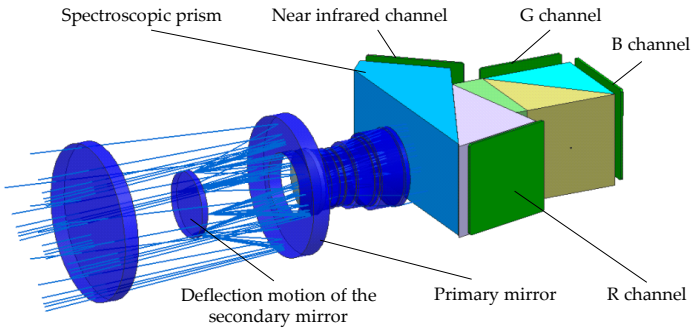

Figure 5. Schematic diagram of the optical system and spectroscopic prisms for the aerial camera.

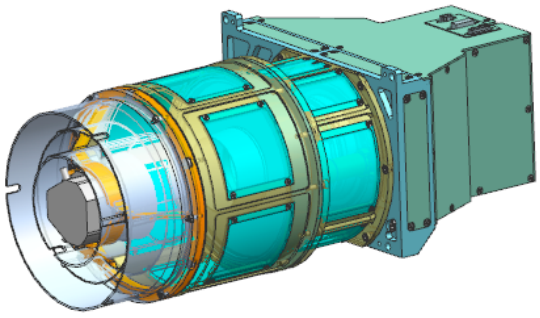

Figure 6. Schematic diagram of aerial camera structure.

In this design case, the image-motion compensation range of ±0.05° was selected based on the deflection angle allowed by the secondary mirror and the angular motion range of the secondary mirror driving mechanism. When the integration time of the optical imaging system was set to 1 ms, the secondary mirror was capable of compensating for the image motion caused by the scanning angular velocity of the aerial camera at 65°/s. The compensation accuracy and compensation speed of the secondary mirror were

contingent upon the control accuracy and compensation bandwidth of the actuator. As shown in Figure 7, when the secondary mirror was deflected to its maximum angle, the coma of the optical system increased by 0.018λ, the astigmatism increased by 0.06λ, and the modulation transfer function decreased by 0.05. However, the modulation transfer function of the optical imaging system was better than 0.28. Although asymmetric astigmatism was introduced into the optical system, the MTF field distribution of the optical system remained symmetrical, which ensured a good aberration field distribution and enabled the achievement of excellent imaging.

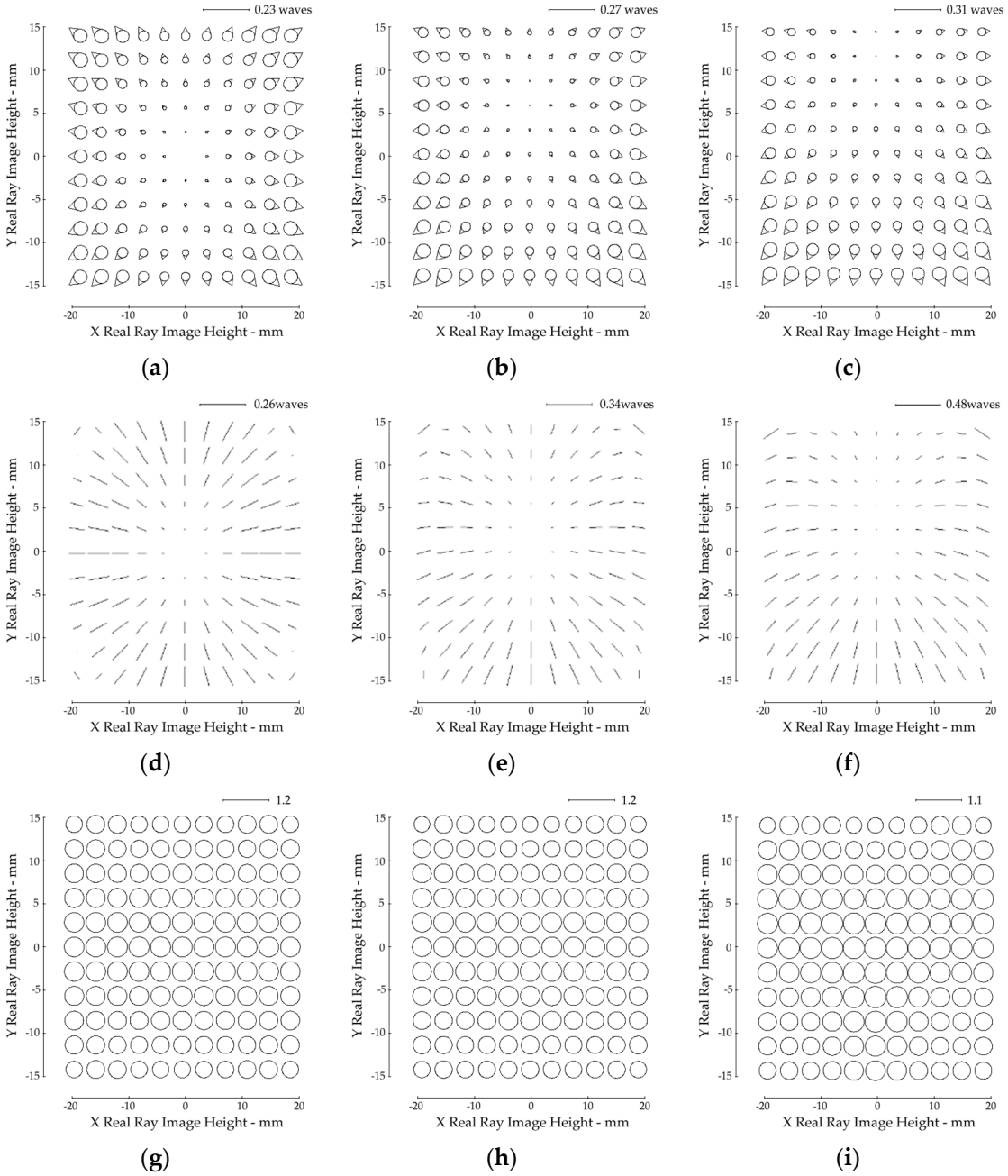

Figure 7. Effect of secondary mirror deflection angle on the aberration field: (**a**) coma aberration field with 0° deflection angle; (**b**) coma aberration field with ±0.03° deflection angle; (**c**) coma aberration field with ±0.05° deflection angle; (**d**) astigmatic aberration field with 0° deflection angle; (**e**) astigmatic aberration field with ±0.03° deflection angle; (**f**) astigmatic aberration field with ±0.05° deflection angle; (**g**) modulation transfer function with 0° deflection angle; (**h**) modulation transfer function with ±0.03° deflection angle; and (**i**) modulation transfer function with ±0.05° deflection angle.

5. Real Experiment

5.1. Image-Motion Compensation Technology Verification Experiment in Laboratory

To adequately validate the image-motion compensation capability of the secondary mirror's image-motion compensation mechanism, an experimental platform was constructed, as illustrated in Figure 8. The instruments used for the image-motion compensation experiment mainly included a collimator and a two-axis scanning platform. By adjusting the pitch and roll scanning rate of the two-axis scanning platform, we accurately simulated the attitude rate of the targets (No. 4 resolution target, cross-target) under different speed-to-height ratios and different scanning rates. Simultaneously, the two-axis image-motion compensation mechanism drove the secondary mirror's motion to compensate for the image motion caused by the target movement. In the experiments, the two-axis scanning platform was scanned at a velocity of +60°/s for the roll and 5°/s for the pitch.

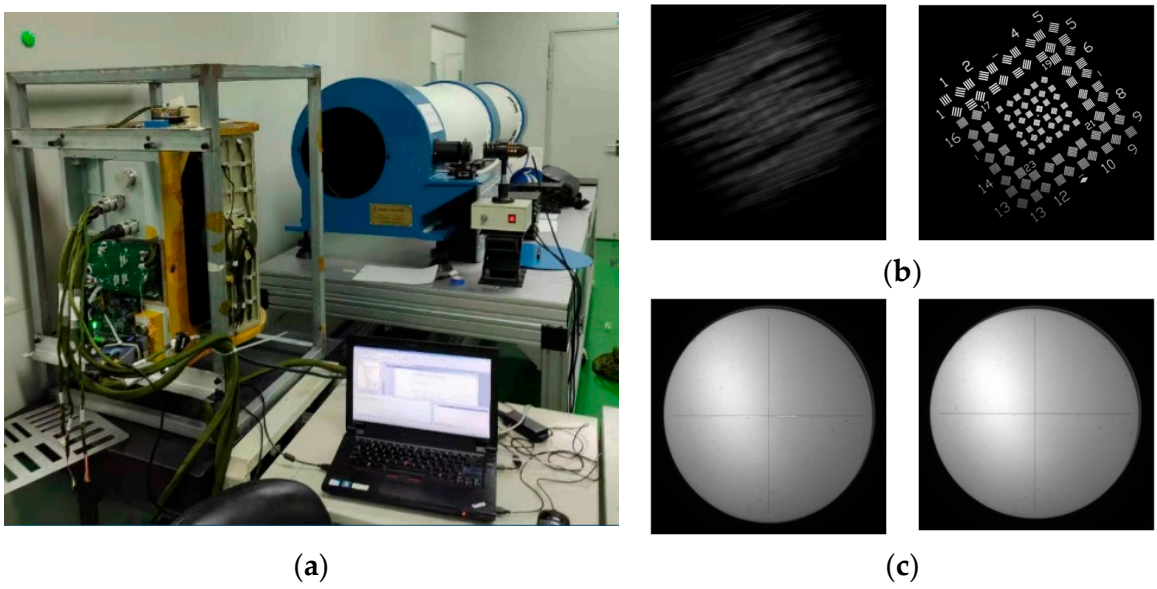

Figure 8. Images of the image-motion compensation experiment: (**a**) the real scene; (**b**) the resolution target images; and (**c**) the cross-target images.

The formula for calculating the aerial camera's ability to distinguish the number of line pairs per millimeter N is as follows:

$$N = \frac{N_0}{f} f_0, \tag{16}$$

where N_0 is the number of line pairs per millimeter of the resolution target that the camera can distinguish. The 11th group of the No. 4 resolution target was selected for this experiment with a value of 11.1 lp/mm. f_0 represents the focal length of the collimator, which has a value of 3000 mm, and f is the focal length of the aerial camera.

According to the above formula, the number of line pairs per millimeter that the aerial camera could dynamically distinguish was 74 lp/mm, which reached the design value. Furthermore, for cross-target imaging, the image centroid offset of the cross-target before and during the experiment was within 0.25 pixels, indicating that the two-dimensional image-motion compensation accuracy was better than 0.5 pixels.

5.2. Flight Experiment with Real Data

To further validate the image-motion compensation capability of the image-motion compensation mechanism, a flight experiment based on actual data was carried out. Figure 9a shows a partial image captured by the carrier at a flight speed of 242 km/h and a flight altitude of 3.17 km, with the aerial camera's roll angle being 4.2° to ground

normal. Figure 9b shows the original image of the resolution target. Figure 9c,d show the zoomed images of the resolution target with the comprehensive image-motion compensation mechanism being on and off, respectively.

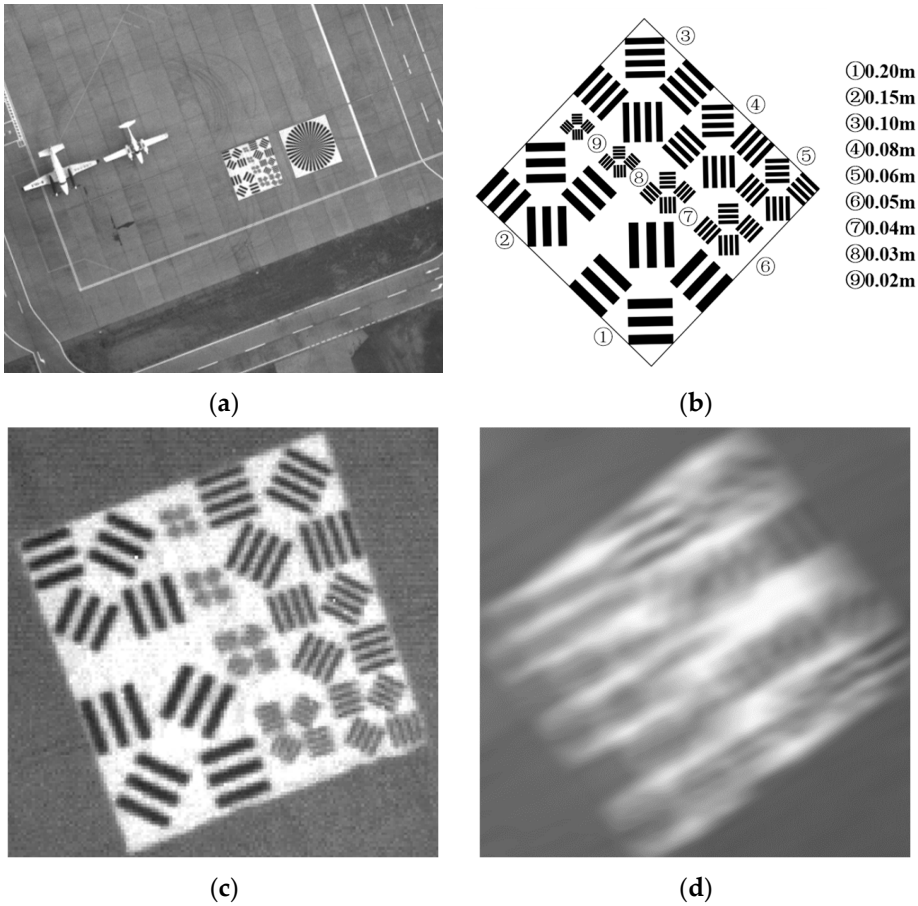

Figure 9. Airport flight experiment: (**a**) partial image of the flight experiment; (**b**) original image of the resolution target; (**c**) zoomed image of the resolution target with the image-motion compensation mechanism turned on; and (**d**) zoomed image of the resolution target with the image-motion compensation mechanism turned off.

Based on the parameters of the flight experiment, the theoretical ground sampling distance can be obtained as follows:

$$GSD_{4.2^\circ} = \left(h / \cos^2 4.2^\circ \Big/ f \right) \times ps = 0.045\text{m}, \tag{17}$$

where $GSD_{4.2^\circ}$ is the theoretical ground sampling distance, and h is flight altitude.

The resolution target depicted in Figure 9b was a 10 m by 10 m square target with a maximum stripe width of 0.2 m and a minimum stripe width of 0.02 m. As can be seen from Figure 9c, the edge of the 0.05 m striped target is relatively clear, and the black and white boundary is obvious, indicating that the aerial camera could clearly distinguish the 0.05 mm striped target, which was very close to the theoretical ground sampling distance. It was proved that the image-motion compensation technology mentioned in this paper met the application requirements of aerial cameras.

Furthermore, to assess the camera's capacity to compensate for image motion, a flight experiment was conducted over an urban environment. Figure 10 illustrates the imaging effects of the four-spectral-band cameras with the image-motion compensation mechanism turned on. The experimental results demonstrate that the movement of the secondary mirror could achieve the image-motion compensation of the four-spectral-band cameras,

which met the design expectations. The obtained R-spectral band image, G-spectral band image, and B-spectral band image could be fused to obtain an RGB color image, as shown in Figure 10e.

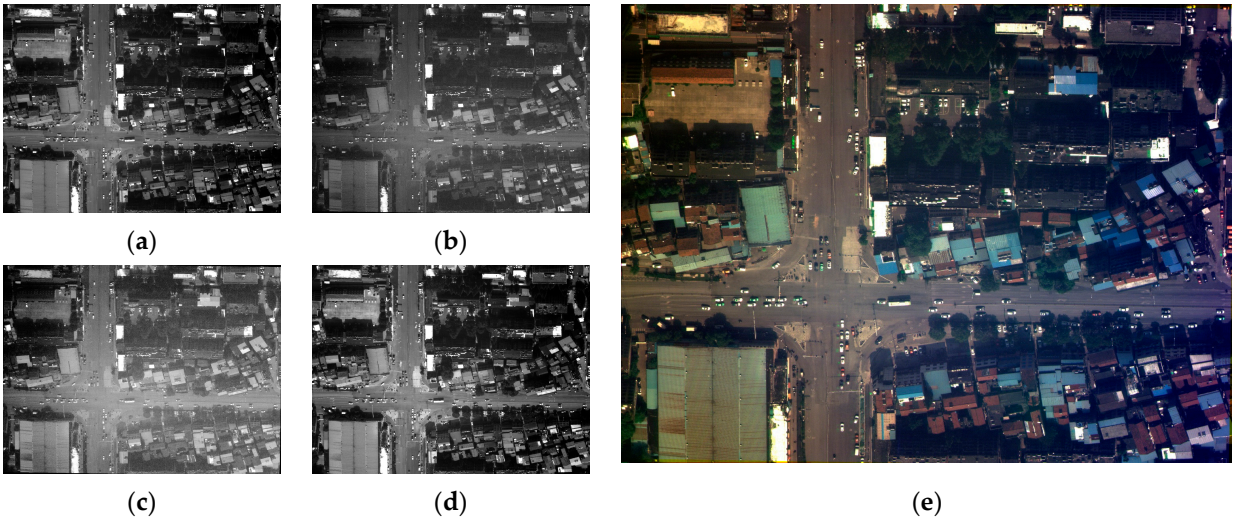

Figure 10. Urban flight experiment imaging results: (**a**) R-spectral band; (**b**) G-spectral band; (**c**) B-spectral band; (**d**) NIR spectral band; and (**e**) RGB image fusion.

According to publicly available information, the image-motion compensation accuracy of the Global Hawk camera, CA-295, DB-110, LOROP, and VisionMap A3 has reached sub-pixel level, typically within the range of 0.1 pixels to 0.5 pixels [33]. This high-precision image-motion compensation enables the above-mentioned aerial cameras to obtain stable and clear images in high-altitude, high-speed flight, and dynamic environments. Furthermore, based on experimental results, the image-motion compensation accuracy based on the technology in this paper is better than 0.5 pixels, which also reaches the advanced level. This paper can provide technical support for the fields of electro-optical reconnaissance and mapping, and can also expand this technology to various types of electro-optical payloads.

6. Conclusions

In this paper, we presented the technical characteristics of the scanning imaging mode for aerial cameras and addressed the issue of image motion resulting from this working mechanism, highlighting the necessity for image-motion compensation in the application of aerial scanning imaging cameras. On this basis, research on the image-motion compensation technology of an aerial camera based on the multi-dimensional motion of the secondary mirror was carried out. The secondary mirror served as the compensatory element for image motion, enabling comprehensive compensation for forward/scanning image motion through its deflection motion. The paper presented an analysis of the effects of the multi-dimensional motion of the secondary mirror on the first-order parameters and the third-order aberration fields, and also provided a design case. To validate the image-motion compensation capability of the secondary mirror's image-motion compensation mechanism, laboratory and flight imaging experiments were carried out. The laboratory experimental results demonstrated that the dynamic resolution of the aerial camera achieved 74 lp/mm through the use of secondary mirror deflection motion for image-motion compensation, and the accuracy of this image-motion compensation method was better than 0.5 pixels. Furthermore, the flight experimental results demonstrated that the aerial camera, based on the multi-dimensional motion of the secondary mirror for image-motion compensation, worked stably, and was capable of acquiring high-quality images. Due to limited conditions, only laboratory and flight imaging experiments have been conducted. Subsequently, the imaging experiment and the verification experiment of the image-motion compensation technology under vacuum conditions will be carried out to facilitate applications in near-

space and space-based environments. In conclusion, the experimental results demonstrate that the integrated design approach for imaging and image-motion compensation is feasible and can be widely applied to the development of ground-based, air-based, near-space, and space-based optical imaging systems.

Author Contributions: Conceptualization, H.Z.; methodology, H.Z.; software, H.Z. and R.Q.; writing—original draft preparation, H.Z.; writing—review and editing, W.C. and H.G.; supervision, W.C. All authors have read and agreed to the published version of the manuscript.

Funding: This research received no external funding.

Institutional Review Board Statement: Not applicable.

Informed Consent Statement: Not applicable.

Data Availability Statement: The data presented in this study are available from the first author or the corresponding author upon reasonable request.

Conflicts of Interest: The authors declare no conflicts of interest.

References

1. Sun, C.; Ding, Y.; Wang, D.; Tian, D. Backscanning Step and Stare Imaging System with High Frame Rate and Wide Coverage. *Appl. Opt.* **2015**, *54*, 4960–4965. [CrossRef] [PubMed]
2. Zhi, Z.; Qu, H.; Tao, S.; Zheng, L.; Ying, S.; Zhu, H. The Design of Cone and Pendulum Scanning Mode Using Dual-Camera with Multi-Dimensional Motion Imaging Micro-Nanosatellite. *Remote Sens.* **2022**, *14*, 4613. [CrossRef]
3. Kraus, M.F.; Potsaid, B.; Mayer, M.A.; Bock, R.; Baumann, B.; Liu, J.J.; Hornegger, J.; Fujimoto, J.G. Motion Correction in Optical Coherence Tomography Volumes on a Per A-scan Basis Using Orthogonal Scan Patterns. *Biomed. Opt. Express* **2012**, *3*, 1182–1199. [CrossRef] [PubMed]
4. Jin, R.; Yu, Y.; Shen, D.; Luo, Q.; Gong, H.; Yuan, J. Flexible, Video-Rate, and Aberration-Compensated Axial Dual-Line Scanning Imaging with Field-of-View Jointing and Stepped Remote Focusing. *Photon. Res.* **2021**, *9*, 1477–1485. [CrossRef]
5. Lyu, W.; Dai, S.; Dong, Y.; Shen, Y.; Song, X.; Wang, T. Attitude Motion Compensation for Imager on Fengyun-4 Geostationary Meteorological Satellite. *Acta Astronaut.* **2017**, *138*, 290–294. [CrossRef]
6. Wang, D.; Li, W.; Yao, Y.; Huang, H.; Wang, Y. A Fine Image Motion Compensation Method for the Panoramic TDI CCD Camera in Remote Sensing Applications. *Opt. Commun.* **2013**, *298–299*, 79–82. [CrossRef]
7. Sun, J.; Ding, Y.; Zhang, H.; Yuan, G.; Zheng, Y. Conceptual Design and Image Motion Compensation Rate Analysis of Two-Axis Fast Steering Mirror for Dynamic Scan and Stare Imaging System. *Sensors* **2021**, *21*, 6441. [CrossRef] [PubMed]
8. Pechatnikov, M.; Shor, E.; Raizman, Y. The New Vision Map A3 Airborne Camera System. In Proceedings of the 52nd Photogrammetric Week, Stuttgart, Germany, 1 September 2009.
9. He, Y.; Peng, J.; Yang, J.; Li, G.; Ling, H.; Cheng, W. Image Motion Analysis and Compensation for Dynamic Push-Broom Imaging with TDI Detectors. *Appl. Opt.* **2024**, *63*, 4819–4829. [CrossRef]
10. Peng, J.; He, Y.; Zheng, L.; Wang, S.; Cheng, W. Analysis of Image Motion for Optical Remote Sensing Satellites Staring Imaging with Area-Array Detectors. *Appl. Opt.* **2023**, *62*, 2470–2478. [CrossRef]
11. Zhang, H. Research on the Calibration Method of Interior Orientation Elements for the Catadioptric Mapping Camera with the Motion of Optical Elements. Ph.D. Thesis, Changchun Institute of Optics, Fine Mechanics and Physics, Chinese Academy of Science, Beijing, China, 2023. (In Chinese).
12. Schmid, T.; Thompson, K.P.; Rolland, J.P. Misalignment-Induced Nodal Aberration Fields in Two-Mirror Astronomical Telescopes. *Appl. Opt.* **2010**, *49*, 131–144. [CrossRef]
13. Gu, Z. Misalignment Corrections in Reflective Telescopes. Ph.D. Thesis, Changchun Institute of Optics, Fine Mechanics and Physics, Chinese Academy of Science, Beijing, China, 2016. (In Chinese).
14. Thompson, K.P.; Schmid, T.; Rolland, J.P. The misalignment induced aberrations of TMA telescopes. *Opt. Express* **2008**, *16*, 20345–20353. [CrossRef] [PubMed]
15. Bai, X.; Ju, G.; Ma, H.; Xu, S. Aberrational interactions between axial and lateral misalignments in pupil-offset off-axis two-mirror astronomical telescopes. *Appl. Opt.* **2019**, *58*, 7693–7707. [CrossRef]
16. Ma, H.; Ju, G.; Zhang, X. Optical Design Method of Two-Mirror Astronomical Telescopes with Reduced Misalignment Sensitivities Based on the Nodal Aberration Theory. *OSA Continuum* **2018**, *1*, 145–161. [CrossRef]
17. Liu, X.; Yuan, D.; Song, L.; Yuan, G.; Zhang, H.; Ding, Y.; Zhang, C. Two-Mirror Aerial Mapping Camera Design with a Tilted-Aplanatic Secondary Mirror for Image Motion Compensation. *Opt. Express* **2023**, *31*, 4108–4121. [CrossRef]
18. Scaduto, L.C.N.; Sasian, J.; Stefani, M.A.; Neto, J.C.D.C. Two-Mirror Telescope Design with Third-Order Coma Insensitive to Decenter Misalignment. *Opt. Express* **2013**, *21*, 6851–6865. [CrossRef]
19. Schmid, T. Misalignment Induced Nodal Aberration Fields and Their Use in the Alignment of Astronomical Telescopes. Ph.D. Thesis, University of Central Florida, Orlando, FL, USA, 2010.

20. Born, M.; Wolf, E. *Principles of Optics: Electromagnetic Theory of Propagation, Interference and Diffraction of Light*, 6th ed.; Pergamon Press, Headington Hill Hall: Oxford, UK, 1980.
21. Bodrov, S.V.; Kachurin, Y.Y.; Kryukov, A.V.; Batshev, V.I. Compact Long-Focus Catadioptric Objective. In Proceedings of the 25th International Symposium on Atmospheric and Ocean Optics: Atmospheric Physics, Novosibirsk, Russia, 18 December 2019. SPIE 11208.
22. Galan, M.; Strojnik, M.; Wang, Y. Design Method for Compact, Achromatic, High-Performance, Solid Catadioptric System (SoCatS), from Visible to IR. *Opt. Express* **2019**, *27*, 142–149. [CrossRef] [PubMed]
23. Shen, Y.; Wang, H.; Xue, Y.; Xie, Y.; Lin, S.; Liu, J.; Liu, M. Compact Catadioptric Optical System with Long Focal Length Large Relative Aperture and Large Field of View. In Proceedings of the AOPC 2020: Telescopes, Space Optics, and Instrumentation, Beijing, China, 5 November 2020. SPIE 11570.
24. Zhang, H.; Chen, W.; Ding, Y.; Qu, R.; Chang, S. Optical System Design of Oblique Airborne-Mapping Camera with Focusing Function. *Photonics* **2022**, *9*, 537. [CrossRef]
25. Qin, Z.; Wang, X.; Ren, C.; Qi, Y.; Meng, Q. Design Method for a Reflective Optical System with Low Tilt Error Sensitivity. *Opt. Express* **2021**, *29*, 43464–43479. [CrossRef]
26. Laikin, M. *Lens Design*, 4th ed.; CRC Press: Boca Raton, FL, USA, 2018.
27. Lim, T.-Y.; Park, S.-C. Design of a Catadioptric System with Corrected Color Aberration and Flat Petzval Curvature Using a Graphically Symmetric Method. *Curr. Opt. Photonics* **2018**, *2*, 324–331.
28. Liu, Z.; Yu, F. Aberration Correction Method for the Catadioptric Imaging System Design. *Appl. Opt.* **2016**, *55*, 2943–2950. [CrossRef]
29. Ryu, T.S.; Park, S.C. Achromatic and Athermal Design Using Cost-Effective Glass Selection and Aberration-Corrected Point Matching on a Glass Map. *Appl. Opt.* **2021**, *60*, 3013–3020. [CrossRef] [PubMed]
30. Xie, N.; Cui, Q.; Sun, L.; Wang, J. Optical Athermalization in the Visible Waveband Using the 1 + ∑ Method. *Appl. Opt.* **2019**, *58*, 635–641. [CrossRef] [PubMed]
31. Zhu, J.; Shen, W. Analytical Design of Athermal Ultra-Compact Concentric Catadioptric Imaging Spectrometer. *Opt. Express* **2019**, *27*, 31094–31109. [CrossRef] [PubMed]
32. Liu, T.; Wang, C.; Yu, Y.; Liu, Z.; He, F. Passive Athermal Optical Design Method Considering Thermal-Induced Surface Deformation. *Photonics* **2021**, *8*, 396. [CrossRef]
33. Wang, Y.; Tian, D. Review of Image Shift and Image Rotation Compensation Control Technology for Aviation Optoelectronic Imaging. *Opt. Precis. Eng.* **2022**, *30*, 3128–3138. [CrossRef]

Disclaimer/Publisher's Note: The statements, opinions and data contained in all publications are solely those of the individual author(s) and contributor(s) and not of MDPI and/or the editor(s). MDPI and/or the editor(s) disclaim responsibility for any injury to people or property resulting from any ideas, methods, instructions or products referred to in the content.